
Using Artificial Intelligence to Model Phase Changes in the Mantle

Preliminary Draft

Buchanan Kerswell



04 July 2023

Contents

1	Introduction	2
1.1	Computational Limitations for Computing Phase Changes in the Mantle	2
2	Computing a Database of Mineral Assemblages and Rock Properties in the Mantle	4
2.0.1	Gibbs Free Energy Minimization Benchmarking Results	4
2.1	PT Conditions in the Upper Mantle	5
2.2	Bulk Compositions of the Upper Mantle	5
3	References	5
4	Appendix	6
4.1	Gibbs Free Energy Minimization Benchmarking Results	6

1 Introduction

1.1 Computational Limitations for Computing Phase Changes in the Mantle

Assuming a pyrolitic composition for Earth's mantle (e.g., Green, 1979; Jagoutz et al., 1979; Sun, 1982), the dominant mineral phases between the Moho and core-mantle boundary (~7–2900 km) are the Mg-Fe-rich minerals olivine, ringwoodite, bridgmanite, and ferropericlase (Ringwood, 1991; Stixrude & Lithgow-Bertelloni, 2012). These phases alone may comprise up to 60–90% of the mineral assemblage in the mantle (Stixrude & Lithgow-Bertelloni, 2012). As pressure increases with depth, a series of discrete phase changes to higher-density mineral assemblages occur (Equation 1, Table 1) that define transition zones in the mantle (Ishii et al., 2018) and strongly impact the dynamics of mantle convection and plate tectonics (e.g., Ringwood, 1991). It is therefore critical to approximate phase changes in large-scale geodynamic codes that simulate mantle convection and plate tectonics.

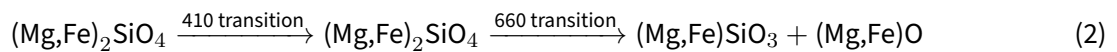
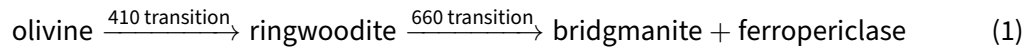


Table 1: Modes and densities of abundant mantle minerals (Stixrude & Lithgow-Bertelloni, 2012).

Mineral	Formula	Structure	Density g/cm ³	% ≤ 660	% > 660
Plagioclase	(Ca, Na)(Al, Si) ₂ O ₈	Triclinic	2.69		
Orthopyroxene	(Mg, Fe) ₂ Si ₂ O ₆	Monoclinic	3.20		
Clinopyroxene	(Mg, Fe, Ca)(Si, Al) ₂ O ₆	Monoclinic	3.40		
Garnet	(Mg, Fe) ₃ Al ₂ Si ₃ O ₁₂	Cubic	3.75		
Spinel	MgAl ₂ O ₄	Cubic	3.65		
Olivine	(Mg, Fe) ₂ SiO ₄	Orthorhombic	3.32		
Wadsleyite	(Mg, Fe) ₂ SiO ₄	Orthorhombic	3.84		
Bridgmanite	(Mg, Fe)SiO ₃	Perovskite	4.10		
Ferropericlase	(Mg, Fe)O	Cubic	3.79		

Even with the simplest parameterizations, however, implementing pressure-temperature-composition-time (PTXt)-dependent phase changes has been intractable for large-scale geodynamic models because

current Gibbs free energy minimization (GFEM) algorithms are computationally expensive and slow to converge on stable solutions (Figure 1). For example, it could take more than 75 hours to compute phase transitions for a single timestep during a geodynamic simulation—assuming a 2D mesh resolution of 900x300 and a 1-second computation time for GFEM at each node (a generous estimate, see Figure 1). Although recent work to parallelize GFEM (Riel et al., 2022) has decreased computation times dramatically (Figure 1), directly coupling GFEM algorithms to geodynamic codes would require computation times on the order of milliseconds or applying parallelization to thousands of cores to be feasible (i.e. a few minutes for a single timestep on a 900x300 resolution mesh). This rate of improvement seems unlikely within the current GFEM paradigm and widespread use of such a tool is unlikely if it requires access to many GPUs or thousands of CPU cores.

To overcome the intractability of implementing PTXt-dependent phase changes in large-scale geodynamic simulations, we propose a novel approach using machine learning (ML) algorithms. We hypothesize that our alternative approach will improve computational efficiency by up to 3 orders of magnitude beyond the state-of-the-art for a range of realistic mantle conditions and rock compositions. Moreover, our proposed approach for improving computational efficiency is generalizable to other datasets, and thus has potential for scaling other computationally-intensive models of Earth processes in the atmosphere, hydrosphere, biosphere and geosphere.

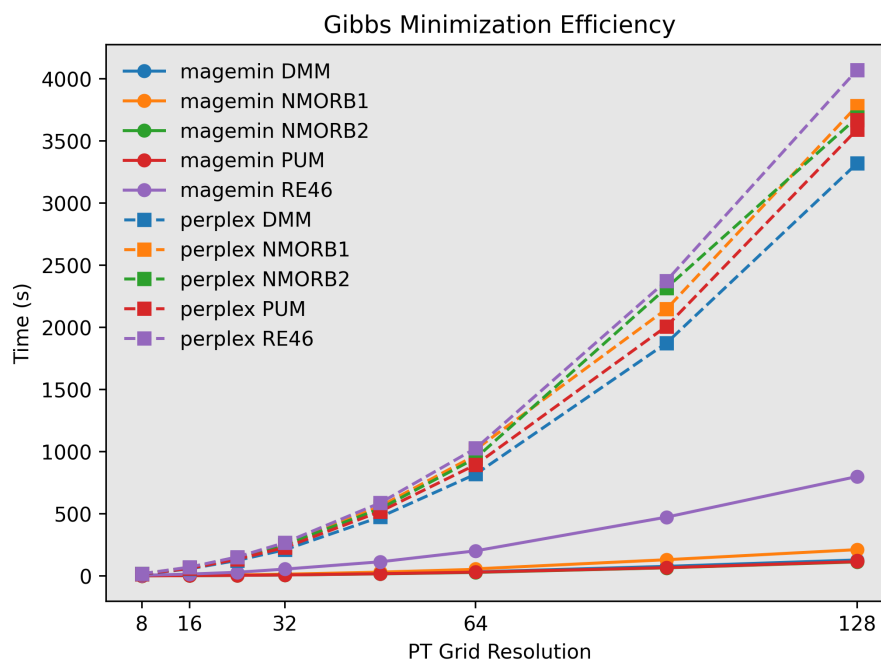


Figure 1: Benchmark results for programs MAGEMin and Perple_X. Note that MAGEMin was ran in parallel on 6 CPU cores, while Perple_X has no parallel capabilities. In the best case, GFEM takes 124 seconds (see Table 3 in Appendix 4.1).

2 Computing a Database of Mineral Assemblages and Rock Properties in the Mantle

2.0.1 Gibbs Free Energy Minimization Benchmarking Results

Samples of various primitive and evolved mantle compositions (Table 2) were used for benchmarking GFEM algorithms implemented in the programs [MAGEMin](#) and [Perple_X](#) (Connolly, 2009; Riel et al., 2022). Table 3 in Appendix 4.1 shows the benchmarking results in terms of computation times. All computations were made on a Macbook Pro (2022; M2 chip) with macOS 13.4 and Python 3.11.4. Note that MAGEMin was ran on 6 CPU cores in parallel, while Perple_X does not have parallel capabilities.

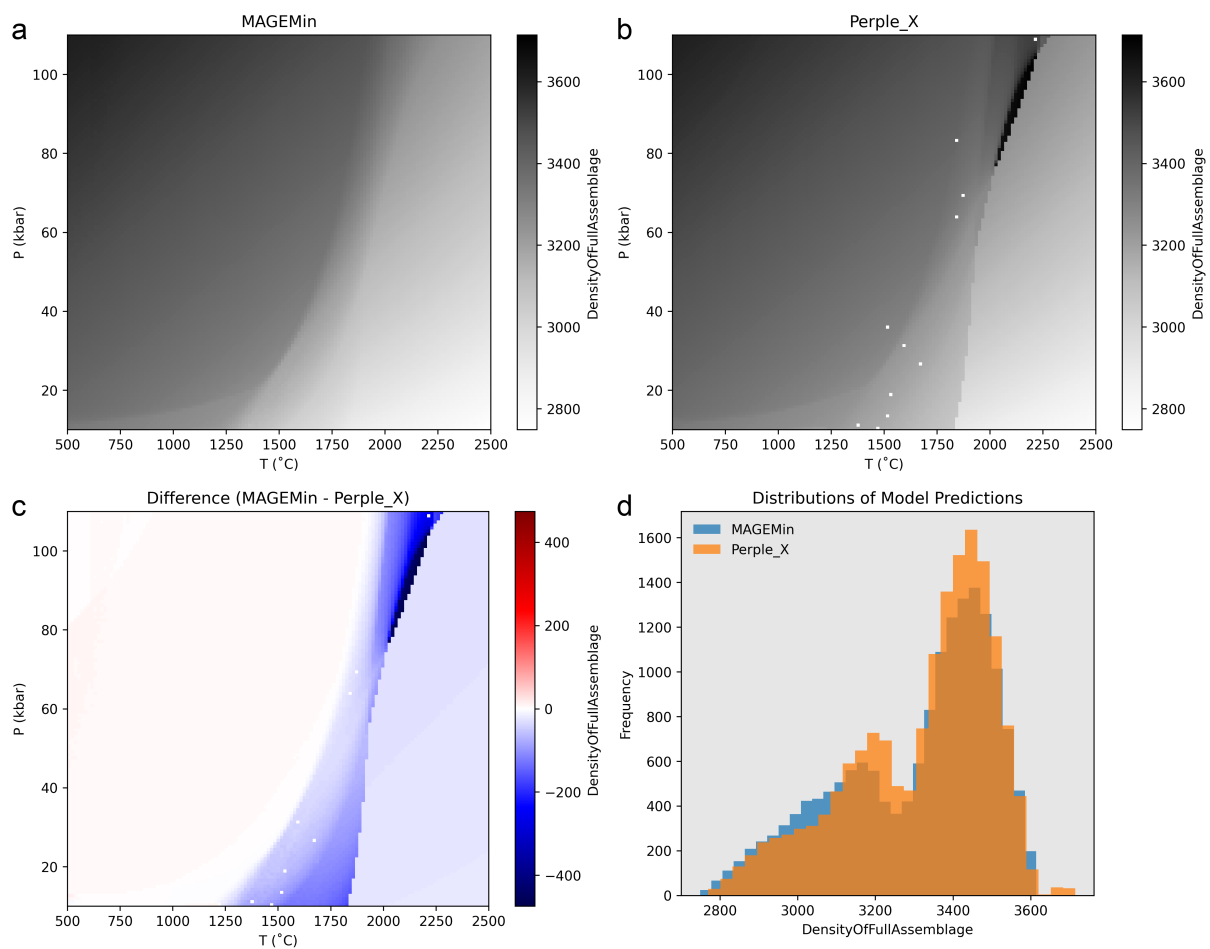


Figure 2: caption

Table 2: Sample compositions (in wt. % oxides) for benchmarking.

Sample	SiO ₂	Al ₂ O ₃	CaO	MgO	FeO	K ₂ O	Na ₂ O	TiO ₂	O ₂	Cr ₂ O ₃	Reference
PUM	44.9	4.44	3.54	37.71	8.03	0.029	0.36	0.2	0.01	0.38	Sun & McDonough (1989)
DMM	44.71	3.98	3.17	38.73	8.18	0.006	0.13	0.13	0.01	0.57	Workman & Hart (2005)
RE46	50.72	9.16	15.21	16.25	7.06	0.010	1.47	0.39	0.35	0.01	Yang et al. (1996)
NMORB53.21		9.41	12.21	12.21	8.65	0.090	2.90	1.21	0.69	0.02	Gale et al. (2013)

2.1 PT Conditions in the Upper Mantle

The PT conditions for this inferred transition are estimated at 23.4 GPa and between 1900–2000 K from experiments and

2.2 Bulk Compositions of the Upper Mantle

3 References

- Connolly, J. (2009). The geodynamic equation of state: What and how. *Geochemistry, Geophysics, Geosystems*, 10(10).
- Gale, A., Dalton, C., Langmuir, C., Su, Y., & Schilling, J. (2013). The mean composition of ocean ridge basalts. *Geochemistry, Geophysics, Geosystems*, 14(3), 489–518.
- Green, D. (1979). Petrogenesis of mid ocean ridge basalts. *The Earth: Its Origin, Structure and Evolution*, 200–299.
- Ishii, T., Huang, R., Fei, H., Koemets, I., Liu, Z., Maeda, F., et al. (2018). Complete agreement of the post-spinel transition with the 660-km seismic discontinuity. *Scientific Reports*, 8(1), 6358.
- Jagoutz, E., Palme, H., Baddenhausen, H., Blum, K., Cendales, M., Dreibus, G., et al. (1979). The abundances of major, minor and trace elements in the earth's mantle as derived from primitive ultramafic nodules. In *In: Lunar and planetary science conference, 10th, houston, tex., march 19-23*,

- 1979, proceedings. Volume 2. (A80-23617 08-91) new york, pergamon press, inc., 1979, p. 2031-2050. Research supported by the deutsche forschungsgemeinschaft. (Vol. 10, pp. 2031–2050).
- Riel, N., Kaus, B., Green, E., & Berlie, N. (2022). MAGEMin, an efficient gibbs energy minimizer: Application to igneous systems. *Geochemistry, Geophysics, Geosystems*, 23(7), e2022GC010427.
- Ringwood, A. (1991). Phase transformations and their bearing on the constitution and dynamics of the mantle. *Geochimica Et Cosmochimica Acta*, 55(8), 2083–2110.
- Stixrude, L., & Lithgow-Bertelloni, C. (2012). Geophysics of chemical heterogeneity in the mantle. *Annual Review of Earth and Planetary Sciences*, 40, 569–595.
- Sun, S. (1982). Chemical composition and origin of the earth's primitive mantle. *Geochimica Et Cosmochimica Acta*, 46(2), 179–192.
- Sun, S., & McDonough, W. (1989). Chemical and isotopic systematics of oceanic basalts: Implications for mantle composition and processes. *Geological Society, London, Special Publications*, 42(1), 313–345.
- Workman, R., & Hart, S. (2005). Major and trace element composition of the depleted MORB mantle (DMM). *Earth and Planetary Science Letters*, 231(1-2), 53–72.
- Yang, H., Kinzler, R., & Grove, T. (1996). Experiments and models of anhydrous, basaltic olivine-plagioclase-augite saturated melts from 0.001 to 10 kbar. *Contributions to Mineralogy and Petrology*, 124(1), 1–18.

4 Appendix

4.1 Gibbs Free Energy Minimization Benchmarking Results

Table 3: Benchmark computation times.

Method	Sample	PT Grid Resolution	Time (s)
magemin	DMM	8x8	1.9
magemin	DMM	16x16	3.4
magemin	DMM	24x24	5.8
magemin	DMM	32x32	8.9
magemin	DMM	48x48	19.2
magemin	DMM	64x64	32.2
magemin	DMM	96x96	76.9

Method	Sample	PT Grid Resolution	Time (s)
magemin	DMM	128x128	128.4
perplex	DMM	8x8	12.7
perplex	DMM	16x16	56.9
perplex	DMM	24x24	124.6
perplex	DMM	32x32	210.5
perplex	DMM	48x48	474.6
perplex	DMM	64x64	819.2
perplex	DMM	96x96	1874.2
perplex	DMM	128x128	3321.7
magemin	NMORB	8x8	1.3
magemin	NMORB	16x16	3.9
magemin	NMORB	24x24	8.1
magemin	NMORB	32x32	13.7
magemin	NMORB	48x48	30.5
magemin	NMORB	64x64	52.9
magemin	NMORB	96x96	130.2
magemin	NMORB	128x128	211.5
perplex	NMORB	8x8	16.5
perplex	NMORB	16x16	68.3
perplex	NMORB	24x24	143.1
perplex	NMORB	32x32	249.9
perplex	NMORB	48x48	560.6
perplex	NMORB	64x64	971.4
perplex	NMORB	96x96	2147.8
perplex	NMORB	128x128	3784.6
magemin	PUM	8x8	0.7
magemin	PUM	16x16	2.0

Method	Sample	PT Grid Resolution	Time (s)
magemin	PUM	24x24	4.3
magemin	PUM	32x32	7.5
magemin	PUM	48x48	17.5
magemin	PUM	64x64	30.1
magemin	PUM	96x96	66.0
magemin	PUM	128x128	124.5
perplex	PUM	8x8	14.9
perplex	PUM	16x16	59.7
perplex	PUM	24x24	134.6
perplex	PUM	32x32	228.4
perplex	PUM	48x48	518.3
perplex	PUM	64x64	895.2
perplex	PUM	96x96	2008.6
perplex	PUM	128x128	3594.6
magemin	RE46	8x8	4.9
magemin	RE46	16x16	14.8
magemin	RE46	24x24	29.2
magemin	RE46	32x32	54.7
magemin	RE46	48x48	113.5
magemin	RE46	64x64	201.7
magemin	RE46	96x96	473.0
magemin	RE46	128x128	800.1
perplex	RE46	8x8	17.5
perplex	RE46	16x16	70.6
perplex	RE46	24x24	152.5
perplex	RE46	32x32	268.0
perplex	RE46	48x48	588.1

Method	Sample	PT Grid Resolution	Time (s)
perplex	RE46	64x64	1027.0
perplex	RE46	96x96	2375.6
perplex	RE46	128x128	4073.3
